



# Effect of Temperature on the Fracture Toughness of a NiTiHf High Temperature Shape Memory Alloy

B. Young<sup>1</sup> · B. Haghgouyan<sup>1</sup> · D. C. Lagoudas<sup>1,2</sup> · I. Karaman<sup>1</sup>

Published online: 2 December 2019  
© ASM International 2019

**Abstract** The fracture toughness of Ni<sub>50.3</sub>Ti<sub>29.7</sub>Hf<sub>20</sub> high temperature shape memory alloy was systematically investigated as a function of temperature. A set of nominally isothermal fracture toughness tests were conducted on disk-shaped compact tension specimens at five temperatures corresponding to three thermodynamical conditions: (i) below martensite finish temperature to obtain the fracture toughness of martensite (ii) above martensite start temperature in austenite but below the martensite desist temperature ( $M_d$ , the temperature above which the austenite does not transform), in order to find the fracture toughness when stress induced martensitic (SIM) transformation takes place close to the crack tip, and (iii) above  $M_d$ , in order to obtain the fracture toughness of austenite. The extent of the inelastic zone near the crack tip was detected using digital image correlation, and the fracture surfaces were examined. The fracture behavior was highly temperature/phase dependent. The fracture toughness of the transforming material was higher than that of austenite and martensite, i.e. SIM transformation acts as a toughening mechanism. This was attributed to the differences in strain hardening behavior in detwinning, martensitic

transformation, and plastic deformation regimes of the stress–strain response, where SIM transformation occurs with the lowest strain hardening rate. The fracture toughness values obtained here are lower than those of equiatomic NiTi.

**Keywords** Fracture toughness · High temperature shape memory alloys · NiTiHf · Phase transformation

## Introduction

Shape memory alloys (SMAs) are high energy density active materials that can undergo repeatable and reversible macroscopic shape changes due to martensitic phase transformation [1]. Since SMAs feature a very high work output for a specific volume as compared to active materials [1], they are promising candidates for replacing existing actuators (e.g. hydraulic or electromagnetic) in weight critical applications [2, 3]. Nickel-titanium (NiTi) is the most commonly known and commercially available SMA, and has seen widespread use in the biomedical industry due to its good biocompatibility, corrosion resistance, and superior mechanical properties [4]. However, the low transformation temperatures of NiTi SMAs have limited their applications as actuators, especially in the aerospace industry, which requires high temperature, actively-controlled actuators. Adding ternary alloying elements to NiTi increases the transformation temperatures to a useable range [5, 6]. In particular, NiTiHf high temperature shape memory alloys (HTSMAs) have been widely explored through several studies focusing on microstructural analysis [7–17], mechanical properties [18–21], fatigue life [22–26], and the effect of processing parameters on microstructure and properties [27–29]. Moreover, the

---

This article is an invited submission to Shape Memory and Superelasticity selected from presentations at the Shape Memory and Superelastic Technology Conference and Exposition (SMST2019) held May 13–17, 2019 at The Bodensee Forum in Konstanz, Germany, and has been expanded from the original presentation.

---

✉ I. Karaman  
ikaraman@tamu.edu

<sup>1</sup> Department of Materials Science and Engineering, Texas A&M University, College Station, TX 77843, USA

<sup>2</sup> Department of Aerospace Engineering, Texas A&M University, College Station, TX 77843, USA

practical viability of NiTiHf HTSMAs has been demonstrated on a test flight as part of an adaptive aircraft structure [30]. However, successful employment of NiTiHf HTSMAs in such applications requires a complete understanding of their crack growth behavior and precise quantification of their fracture properties. To the best of the authors' knowledge, there is no work in the literature reporting fracture toughness of NiTiHf based HTSMAs in the temperature range that covers all possible material states. Moreover, it is not clear whether these ternary SMAs are tougher than NiTi binary alloys or not.

In literature, the majority of studies on the fracture of SMAs [31–41] have reported the fracture toughness of NiTi using ASTM E399 [42], which is based on linear elastic fracture mechanics (LEFM). However, most of the reported experiments in such studies do not satisfy the small-scale yielding condition, which is required for the validity of LEFM. Additionally, because the presence of phase transformation alters near-tip mechanical fields [43–48], SMAs do not conform to conventional elasto-plasticity, and therefore elasto-plastic fracture mechanics (EPFM) cannot be used to characterize the crack growth behavior and predict fracture in SMAs. Recently, there have been efforts [49, 50] to obtain the fracture properties of NiTi using the full-field displacement data, obtained from digital image correlation (DIC). Unlike the standard testing methods, which are used to determine the fracture toughness from load–displacement data, this method requires relatively sophisticated testing setup and rigorous post processing. In an attempt to address some of these challenges, a new methodology described in [51] modifies the existing ASTM E1820 standard [52] to take into account the transformation- and reorientation-induced changes in the elastic properties.

Because the constitutive response of the SMAs is sensitive to temperature, even small variations in temperature may further complicate the study of their fracture behavior. Consequently, quantifying fracture properties of SMAs can be challenging compared to conventional metals. Although fracture properties of NiTi SMAs have been reported in many studies over the years, there seems to be a lack of consensus on the effects of temperature/phase transformation on their fracture toughness [31, 34, 51, 53, 54], in particular on whether martensitic transformation provides a toughening effect or not. For example, Holtz et al. [31] and Maletta et al. [54] reported that fracture toughness increases monotonically with temperature in NiTi SMAs. However, the results of Gollerthan et al. [34] and Haghgouyan et al. [51] demonstrated that the fracture toughness of NiTi binary SMAs is a stepwise function, with fully martensitic materials and materials transforming from austenite to martensite having the same fracture toughness, and the austenite phase above martensite desist

temperature,  $M_d$ , exhibiting higher fracture toughness. Clearly, there is a need to systematically investigate the fracture behavior of new NiTiHf HTSMAs at different temperatures, especially in the martensitic transformation range.

There are only two reported studies on the fracture and crack growth behavior of NiTiHf HTSMAs [55, 56]. In the recent study by the authors, the fracture of an aged martensitic NiTiHf has been investigated under mode-I nominally isothermal loading. Using a disk-shaped compact tension (DCT) specimen, fracture toughness was measured at room temperature (below martensite finish temperature,  $M_f$ ) [55]. Unstable crack growth was observed due to the limited extent of dissipation mechanisms near the crack-tip. The results showed that the fracture toughness of martensitic NiTiHf is relatively lower than that of binary NiTi SMAs. Amin-Ahmadi et al. [56] studied crack propagation mechanisms in an aged NiTiHf HTSMA using post-mortem microstructure characterizations. Transmission electron microscopy (TEM) micrographs showed that cracks propagate mainly along the  $\langle 011 \rangle$  type II twin planes, switching between the twin planes to avoid nano-sized H-phase precipitates.

In the present study, we present the first investigation into the fracture toughness of a NiTiHf HTSMA at different temperatures and phases: (i) below  $M_f$  in fully martensitic state (ii) above martensite start temperature,  $M_s$ , where the stress induced martensitic (SIM) transformation takes place, and (iii) above  $M_d$  in fully austenitic state. Microstructural characterization, near tip strain field measurements, and post-mortem fracture surface analyzes have been performed. The fracture toughness values of the NiTiHf HTSMA were determined at five different temperatures. It was observed that the martensite phase exhibits the lowest fracture toughness and SIM transformation provides a significant toughening effect leading to a higher fracture toughness in the martensitic transformation regime than that of both austenite and martensite phases. The deformation and strain hardening behavior observed in the uniaxial tension experiments shed some light into the potential reasons for the observed differences in the evolution of fracture toughness values with temperature.

## Experimental Methods

### Material

Elemental Ni, Ti, and Hf (99.98%, 99.95% and 99.9% in purity, respectively) were used to fabricate Ni<sub>50.3</sub>Ti<sub>29.7</sub>Hf<sub>20</sub> (at.%) HTSMA via vacuum skull melting under partial argon atmosphere. The material was vacuum homogenized at 1050 °C for 72 h and furnace cooled down to room

temperature. Finally, the homogenized ingot was sealed in a mild steel can and hot extruded at 900 °C. The transformation temperatures of the hot extruded material were measured using differential scanning calorimetry (DSC) and determined using the intersecting tangent lines method to be  $M_f = 125.6$  °C,  $M_s = 152.7$  °C,  $A_s = 163.1$  °C and  $A_f = 183.6$  °C, where  $A_s$  and  $A_f$  indicate austenite start and finish temperatures, respectively (Fig. 1a).

### Microstructural Characterization

Because the microstructure of SMAs is extremely important in controlling their thermomechanical response [11, 25, 34, 57–59], in particular their fracture behavior [23, 35, 60, 61], the oxide content, the size and distribution of oxides, and other microstructural features, including the existence of H-phase precipitates [9], were investigated using scanning electron microscopy (SEM) and TEM. In Fig. 2a, the backscattered electron image shows the white hafnium oxides decorating the grain boundaries. In Fig. 2b, the size distribution of oxides is shown, seen to skew left with a tail to the right, indicating mostly small particles (under  $1 \mu\text{m}^2$ ). In Fig. 2c, a bright field TEM image and corresponding selected area diffraction pattern (SADP) are presented. The TEM image and the diffraction pattern do not provide an evidence for the existence of H-phase precipitation. In the bright field image, there are no clear second-phase particles, and in the SADP, there is no diffuse scattering around the martensite spots that would indicate either the precursor to the H-phase precipitates or

the precipitates themselves. These images were captured on the [100] zone axis of B19'.

### Uniaxial Tensile Experiments

For tensile experiments, dog-bone geometry samples, with the gage dimensions of  $8 \times 3 \times 1 \text{ mm}^3$ , were cut using wire Electrical Discharge Machining (EDM), and tested to failure with an engineering strain rate of  $5 \times 10^{-4} \text{ s}^{-1}$  on a servo-hydraulic MTS test frame equipped with a high-temperature MTS extensometer. The extensometer was directly attached to the gage section of the samples. These samples were loaded in nominally isothermal conditions in order to determine their mechanical properties at different temperatures. The testing temperatures were decided based on the transformation temperatures so that fully martensitic, martensitically transforming, and fully austenitic materials would all be tested. For martensitic materials, two experiments were performed below  $M_f$  ( $M_f - 100$  °C,  $M_f - 25$  °C) at 25 °C and 100 °C. For the samples which are martensitically transforming under stress, the experiments were performed at 160 °C and 200 °C ( $A_s - 5$  °C,  $A_f + 15$  °C), which are above  $M_s$ , but below  $M_d$ . For the experiments at 160 °C, the samples were first heated above  $A_f$  and then cooled down to the test temperature to ensure the starting phase of the experiment is full austenite. The austenitic material was tested above  $M_d$  at 360 °C ( $A_f + 175$  °C).

### Fracture Toughness Experiments

Following the ASTM Standard E1820 [52], DCT specimens, with the width  $W = 20$  mm and the thickness  $B = 3.25 \pm 0.25$  mm, were tested at five different temperatures, 25 °C, 100 °C, 160 °C, 200 °C, and 360 °C, similar to the uniaxial tension experiments, to measure the fracture toughness at different temperature regimes. The specimens were first polished on both sides with abrasive paper down to 1200 grit. The specimens were then cycled sinusoidally at 10 Hz at room temperature with an MTS servo-hydraulic frame (810 Material Test System) under load control, with the load ratio of  $R = P_{\min}/P_{\max} = 0.1$ , in order to grow a fatigue pre-crack. After pre-cracking, all crack length-to-width ratios ( $a/W$ ) were within the  $0.45 < a/W < 0.55$  range. Two experiments were performed at each testing temperature.

For the fracture toughness experiments, the specimens were loaded in displacement control at a rate of  $7.5 \times 10^{-3} \text{ mm/s}$ , following the procedures in ASTM Standard E1820 [52]. To capture the specimen's compliance throughout the experiments, partial unloads and reloads were performed by decreasing the displacement by 0.05 mm at 0.15 mm intervals, a range recommended by

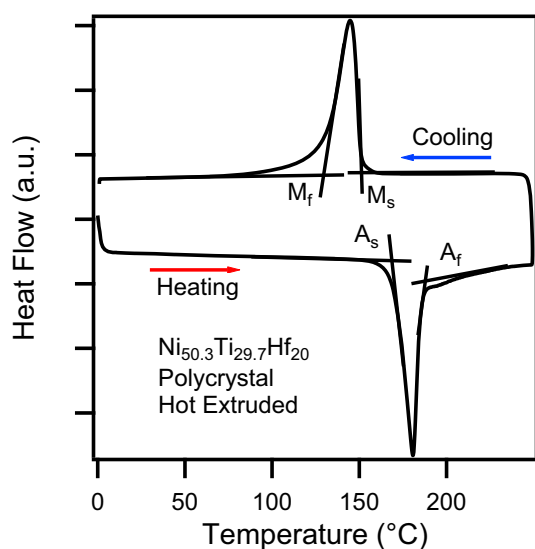


**Fig. 1** Differential scanning calorimetry of a hot extruded, polycrystalline  $\text{Ni}_{50.3}\text{Ti}_{29.7}\text{Hf}_{20}$  high temperature shape memory alloy, revealing transformation temperatures to be  $M_f = 125.6$ ,  $M_s = 152.7$ ,  $A_s = 163.1$ ,  $A_f = 183.6$  °C

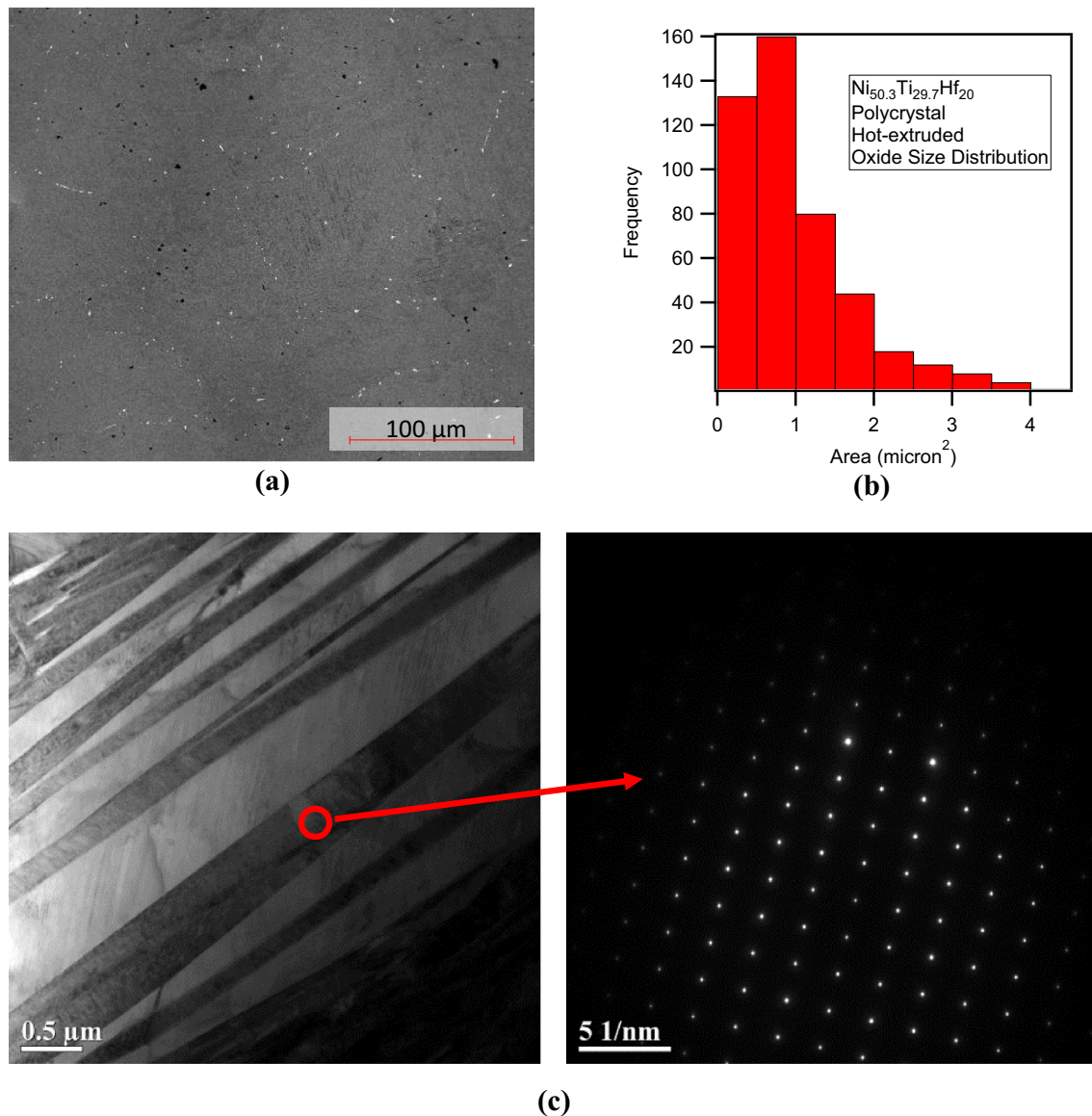


**Fig. 2 a** A back scattered electron image of the hot extruded, polycrystalline  $\text{Ni}_{50.3}\text{Ti}_{29.7}\text{Hf}_{20}$  high temperature shape memory alloy. Hafnium oxides are seen in white, decorating the grain boundaries of the sample; **b** the size and frequency of the oxide distribution, showing a skewed distribution with a tail to the right;

**c** the bright field TEM image, taken on the [100] zone axis, of martensite lathes and corresponding selected area diffraction pattern (SADP). Neither the bright field image nor the SADP show any indication of precipitates

the ASTM Standard E1820. The load and crosshead displacement were recorded continuously at a rate of 10 Hz throughout the experiments. The crosshead displacement was then converted to load line displacement (LLD) using a method introduced in [51], while removing the effect of machine compliance. For the experiments at elevated temperatures, the samples were heated with a Roy 1500 induction heater controlled by a Eurotherm 2200 PID temperature controller. The temperature of the sample was measured by averaging the readings from 6 K-type thermocouples directly spot-welded onto the sample.

Temperatures were recorded in a LabView program through a Measurement Computing data acquisition board.

### In Situ Optical Imaging

Over the course of the experiments, optical images were recorded at a rate of 1 fps using a Point Grey Blackfly camera with a Canon 18–55 mm lens. These images were used to monitor the crack size and measure the 2-D strain distribution using DIC. DIC was chosen because of its non-contact nature. In order to perform DIC, the samples were spray painted with either high-temperature-resistant black

paint and speckled with white or vice versa. The imaging was performed at a resolution of 0.14 mm per pixel. The VIC-2D software, developed by Correlated Solutions, was used to calculate the full-field Lagrangian strains.

## Results and Discussion

### Uniaxial Mechanical Response

The uniaxial tensile test results at different temperatures are presented in Fig. 3a. Starkly different stress–strain responses near the transformation temperatures are clear, which is typical for SMAs. However, the response of the present NiTiHf HTSMA is subtly different than conventional binary NiTi SMAs, as described below. Although it is not the main focus of the current work, in the following, we briefly discuss possible deformation mechanisms that can be responsible for these differences. Understanding the deformation mechanisms during uniaxial loading at different temperatures is expected to help shed some light on the reasons for the evolution of fracture toughness with temperature (“Fracture Toughness Evolution as a Function of Temperature” section below).

For the two experiments below  $M_f$  (25 °C and 100 °C), upon loading, the self-accommodated martensite deforms elastically before undergoing martensite reorientation/detwinning. Then, the samples fail during reorientation/detwinning, probably before the reorientation process is completed. It is worth noting that the stress required to detwin the martensite is lower at 100 °C than that at 25 °C. The detwinning region has a high strain hardening slope ( $11 \pm 1$  GPa), which indicates the difficulty of detwinning and likelihood of simultaneous plastic deformation. In

contrast, SIM transformation region (experiments at 160 °C and 200 °C) features a lower strain hardening slope (5 GPa) than the detwinning region. The very high strain hardening rate observed in the deformation of the martensite phase in the present NiTiHf alloy is quite different than what is observed in binary NiTi, and it is mostly due to the difficulty of detwinning in NiTiHf HTSMAs [62, 63].

In the 160 °C and 200 °C cases, three stages of inelastic deformation can be distinguished. In the first stage, the austenite transforms into SIM. Upon further loading, the SIM is elastically deformed, however, in this second stage, there must be other deformation modes in play since the slope of the stress–strain curves in this stage is significantly lower than what would be expected only from elastic deformation. At the end of the second stage, the onset of a third stage is obvious at both 160 °C and 200 °C. However, the third stage is much clearer in the samples tested at 200 °C due to the extended strain observed in this stage at 200 °C. In fact, the observation of such high tensile ductility at 200 °C is somewhat surprising since in general, many of the Ni-rich NiTiHf and NiTiZr compositions have not been reported to exhibit such high tensile ductility [10, 14–17, 62]. The relatively high ductility should be a consequence of the combination of SIM, detwinning, and inelastic deformation of SIM. It is worth noting that at 200 °C, upon unloading at low strain values (the first stage), the samples show perfect superelasticity (not shown here).

Lastly, in the experiments performed at 360 °C, the austenite phase exhibits conventional plastic deformation behavior with decreasing strain hardening response under increasing applied strain until failure. Although it needs to be confirmed microscopically, the periodic load drops

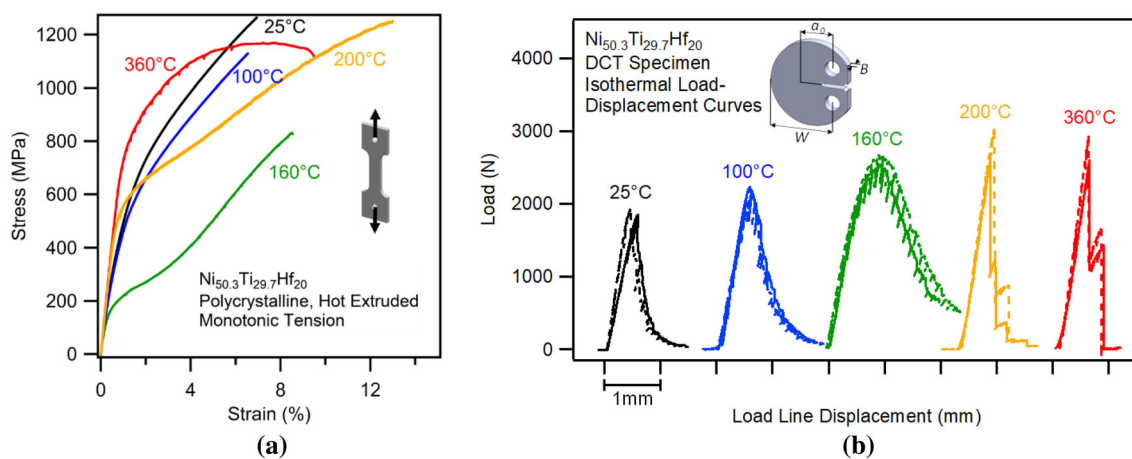


**Fig. 3** Uniaxial tension and mode-I fracture toughness results of hot extruded, polycrystalline  $\text{Ni}_{50.3}\text{Ti}_{29.7}\text{Hf}_{20}$  high temperature shape memory alloy at 25 °C ( $M_f$ -100 °C), 100 °C ( $M_f$ -25 °C), 160 °C ( $A_s$ -5 °C), 200 °C ( $A_f$  + 15 °C), and 360 °C ( $A_f$  + 175 °C): **a** stress–

strain response of dog-bone shaped specimens under tension; **b** load–displacement response of the disk-shaped compact tension (DCT) specimens (thickness  $B = 3.25 \pm 0.25$  mm, width  $W = 20$  mm, initial crack length  $a_0 = 10 \pm 1$  mm)

observed in the stress–strain response at 360 °C (Fig. 3a) can be a consequence of deformation twinning in austenite, the typical deformation mechanism observed in the austenite phase of high strength binary NiTi [62, 64–67]. From all of these stress–strain curves, it can be seen that there is a notable difference in the material behavior depending on whether the samples experience martensite reorientation/detwinning or SIM transformation—the samples strain-harden significantly more when the martensite detwins than what is observed during the SIM transformation.

### Fracture Toughness Evolution as a Function of Temperature

The experimental load–displacement curves obtained from the DCT specimens are presented in Fig. 3b at the same temperatures that the uniaxial mechanical responses were determined. The initial crack lengths in all specimens were  $a_0 = 10 \pm 1$  mm. The load drops on the load–displacement curves come from the unload-reload sequences used to measure the compliance in cases where stable crack growth was observed. In the martensite phase (at 25 °C and 100 °C), unstable crack growth was observed after reaching the load maximum. In the experiments at 160 °C, the material had a greater deviation from linearity and an extended displacement range beyond the load maximum before the complete failure occurred. At 200 °C, the material reached a load maximum without stable crack growth, and failed in an unstable manner. In the case of the purely austenitic material (360 °C), the drop from maximum load was sudden. The load drops at 25 °C and 100 °C were more gradual than those in the 200 °C and 360 °C cases.

Fracture toughness values at each testing temperature were determined from the corresponding load–displacement data, by employing the modified  $J$ -integral method as the fracture criterion, proposed in Ref. [51]. For the samples that exhibited fracture instability, i.e. at 25 °C, 100 °C, 200 °C, and 360 °C, the single-point  $J$  method was implemented where the  $J$ -value at the maximum load is calculated as the sum of elastic and inelastic components:

$$J = J^{\text{el}} + J^{\text{in}} = \frac{\eta^{\text{el}} A^{\text{el}}}{Bb} + \frac{\eta^{\text{in}} A^{\text{in}}}{Bb},$$

where  $b$  is the length of the unbroken ligament,  $A^{\text{el}}$  and  $A^{\text{in}}$  are the elastic and inelastic components of the area under the load–displacement curve, respectively,  $\eta^{\text{el}}$  and  $\eta^{\text{in}}$  are geometry-dependent factors.

For the samples that experienced stable crack growth, i.e. at 160 °C, the  $R$ -curve method was used where the  $J$ -value at the  $i$ th unload/reload sequence is calculated as  $J_i = J_i^{\text{el}} + J_i^{\text{in}}$  where  $J_i^{\text{el}}$  and  $J_i^{\text{in}}$  are the incremental elastic

and inelastic components of  $J_i$ , respectively. Also, crack extension,  $\Delta a$ , was calculated at each unload/reload sequence using the specimen compliance. The critical  $J$ -value was then obtained from the intersection of a regression line to  $J$ - $\Delta a$  data and an offset line at 0.2 mm. More details on the aforementioned methods can be found in Ref. [51]. At 25 °C, 100 °C, 200 °C, and 360 °C, using the single point  $J$  method, an average fracture toughness  $J_Q$  of 35.3, 50.7, 56.4, and 43.1 kJ/m<sup>2</sup> were determined for these four temperatures, respectively. For the samples tested at 160 °C, an average  $J_Q$  value is calculated, using the constructed  $R$ -curve (Fig. 4) as 84.8 kJ/m<sup>2</sup>. These  $J_Q$  values representing the fracture toughness are plotted in Fig. 5 as a function of the temperature.

Up to now, all of the fracture toughness values have been designated as  $J_Q$ . The  $J_Q$  value can be qualified as geometry-independent fracture toughness,  $J_C$ , which is the material property, if the specimen meets thickness and unbroken ligament conditions, given by the equation  $B, b_0 > N(J_Q/2\sigma_Y)^2$  [52], where  $b_0$  is the initial unbroken ligament,  $N$  is a constant, which is 10 or 100, depending on if the  $R$ -curve or single point  $J$  method is used, respectively, and  $\sigma_Y$  is the average of the critical stress (the stress for the onset of reorientation/detwinning, the transformation, or conventional plastic yield stress), and ultimate tensile strength. The experiments at 160 and 360 °C do satisfy the thickness requirements to qualify  $J_Q$  as  $J_C$ , and the experiments at all other temperatures do not.

Although the experiments at 25 °C, 100 °C, and 200 °C do not satisfy thickness requirements according to ASTM

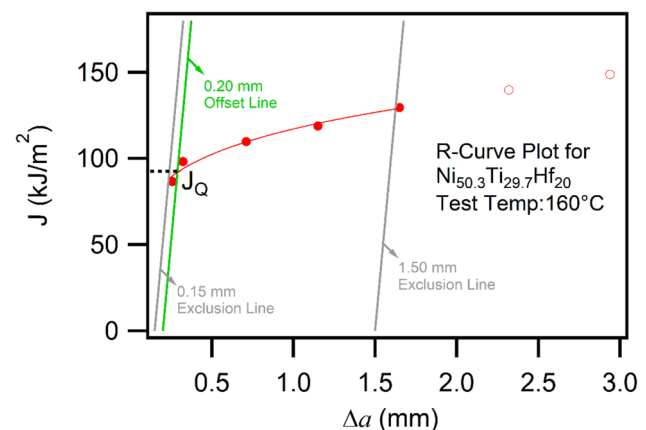


**Fig. 4**  $R$ -curve construction for the fracture toughness experiment at 160 °C for the hot extruded, polycrystalline  $\text{Ni}_{50.3}\text{Ti}_{29.7}\text{Hf}_{20}$  high temperature shape memory alloy. The critical value of  $J_Q$ , shown by the dashed line, is obtained from taking the intercept of a power law regression line of the  $J$ - $\Delta a$  data and a 0.2 mm offset line with a slope of  $2\sigma_Y$ . Here  $\sigma_Y$  is the average of the transformation stress and ultimate tensile strength at the test temperature. Points to the left of the 0.15 mm exclusion line and to the right of the 1.50 mm exclusion line are not used for regression analysis to obtain the power law regression line

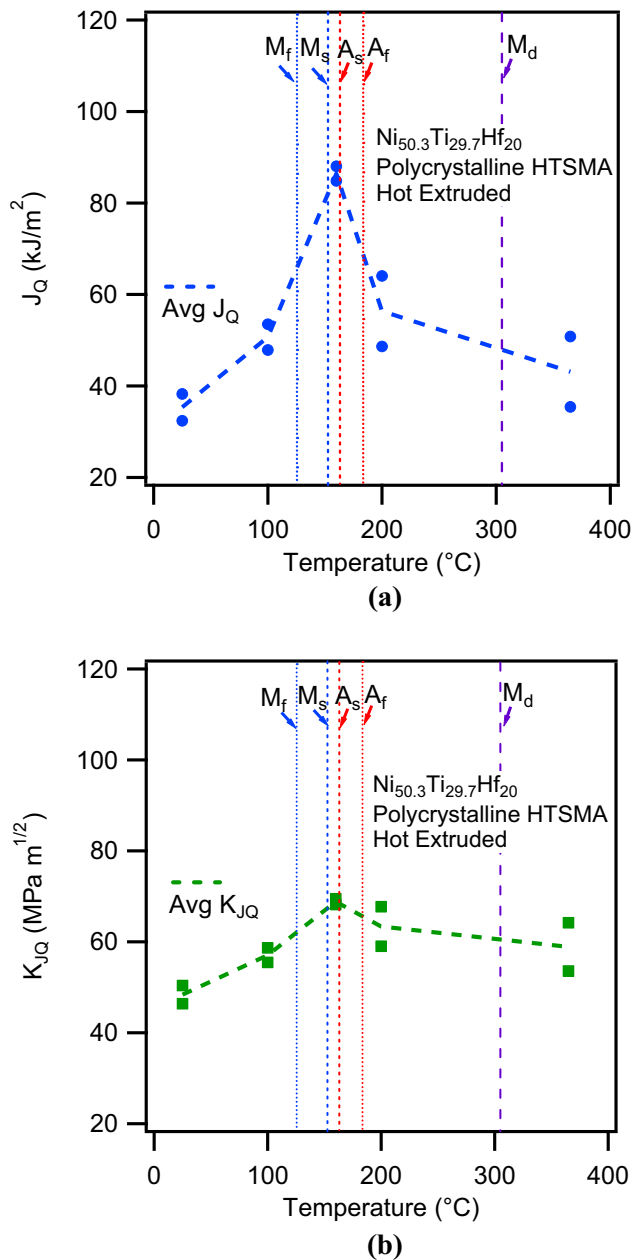


**Fig. 5** **a** Fracture toughness  $J_Q$  vs. temperature; and **b** fracture toughness  $K_{JQ}$  vs. temperature for the hot extruded, polycrystalline Ni<sub>50.3</sub>Ti<sub>29.7</sub>Hf<sub>20</sub> high temperature shape memory alloy. See text for detailed description of how these values were determined from the load displacement curves in Fig. 3b. The SIM transformation appears to have a toughening effect on the fracture toughness in both  $J_Q$  and  $K_{JQ}$ . The material at 200 °C has a less pronounced toughening effect because the stress required to induce transformation at that temperature is higher than that at 160 °C

E1820, the thickness range utilized in this study is of practical importance especially for aerospace applications [68, 69]. Therefore, this study determines the  $J_Q$  values as a function of temperature for the first time for NiTiHf HTSMAs, which can be utilized to identify the failure limits for the given thickness range. Moreover, as discussed

in [70], the required thickness to ensure a thickness-independent fracture toughness for SMAs is not expected to be as stringent as the thickness requirement for conventional ductile materials. Nevertheless, further investigations on the effects of thickness on the fracture of HTSMAs are desirable.

In order to take into account the change in the elastic moduli of SMAs with temperature, the calculated  $J_Q$  values are converted to  $K_{JQ}$  values with  $K_{JQ} = \sqrt{J_Q E}$ , where  $E$  is the temperature dependent elastic modulus. The  $K_J$  values are plotted as a function of temperature in Fig. 5b, and all  $E$ ,  $J_Q$ , and  $K_{JQ}$  values are tabulated in Table 1. Based on Fig. 5, it can be seen that the SIM transformation in the present NiTiHf HTSMA clearly acts as a toughening mechanism due to the energy dissipated by martensitic transformation. This can be seen through the higher values of  $J_Q$  and  $K_{JQ}$  at 160 °C and 200 °C where SIM transformation occurs. SIM transformation has a greater effect on the fracture toughness at 160 °C because the stress needed to start the transformation is lower at 160 °C than at 200 °C, which agrees with the Clausius–Clapeyron relation. Similarly, the higher fracture toughness at 100 °C compared to that at 25 °C can be explained by the lower stress required to detwin the martensite at 100 °C, as mentioned in “Uniaxial Mechanical Response” section.

In contrast to Fig. 5, in the binary equiatomic NiTi SMA [51], the fracture toughness appears to be a stepwise function as a function of temperature, i.e. the fracture toughness of martensite phase and the material that experiences SIM transformation is lower than the fracture toughness of plastically deforming austenite phase. This is the case because the crack propagates in martensite—if the material begins in austenite, it first transforms to martensite and the crack progresses through the transformed martensite region. Therefore, the measured fracture toughness represents the fracture toughness of martensite, regardless of the starting phase whether it is martensite or austenite which transforms to martensite upon loading. The fracture

**Table 1** Apparent elastic modulus ( $E$ ), average  $J_Q$ , and average  $K_{JQ}$  values at different test temperatures for the hot extruded, polycrystalline Ni<sub>50.3</sub>Ti<sub>29.7</sub>Hf<sub>20</sub> high temperature shape memory alloy

Temperature (°C)	$E$ (GPa)	$J_Q$ (kJ/m <sup>2</sup> )	$K_{JQ}$ (MPa√m)
25	66.4	35.3	48.4
100	64.3	50.7	57.1
160	54.8	86.4	68.0
200	71.6	56.4	63.4
360	81.1	43.1	58.9

toughness for austenite is different above  $M_d$  because the material no longer undergoes SIM transformation.

It is believed that the reason for the differences in the fracture toughness in the present NiTiHf of the martensite phase and austenite phase, which transforms into martensite under stress in the transformation temperature range, is the difference in the energies absorbed during the reorientation/detwinning and the SIM transformation processes. In equiatomic NiTi, the detwinning process absorbs a similar amount of energy as the transformation [51], thus, similar fracture toughness values are observed. In the present NiTiHf, the strain hardening rate ( $11 \pm 1$  GPa) in the detwinning region of martensite phase is much higher than that during the transformation (5 GPa) (Fig. 3a),

leading to a smaller inelastic deformation zone at the crack tip. In contrast the SIM transformation leads to a higher fracture toughness and a larger inelastic deformation zone at the crack tip, as experimentally demonstrated in the next section. Under similar load values, the SIM transformation dissipates more energy as compared to the detwinning process.

### Evaluation of Inelastic Deformation Zone at the Crack Tip using DIC

DIC was used to quantify the 2-D strain distributions near the crack tip. At each testing temperature, the deformed image was obtained at the onset of crack growth. For the

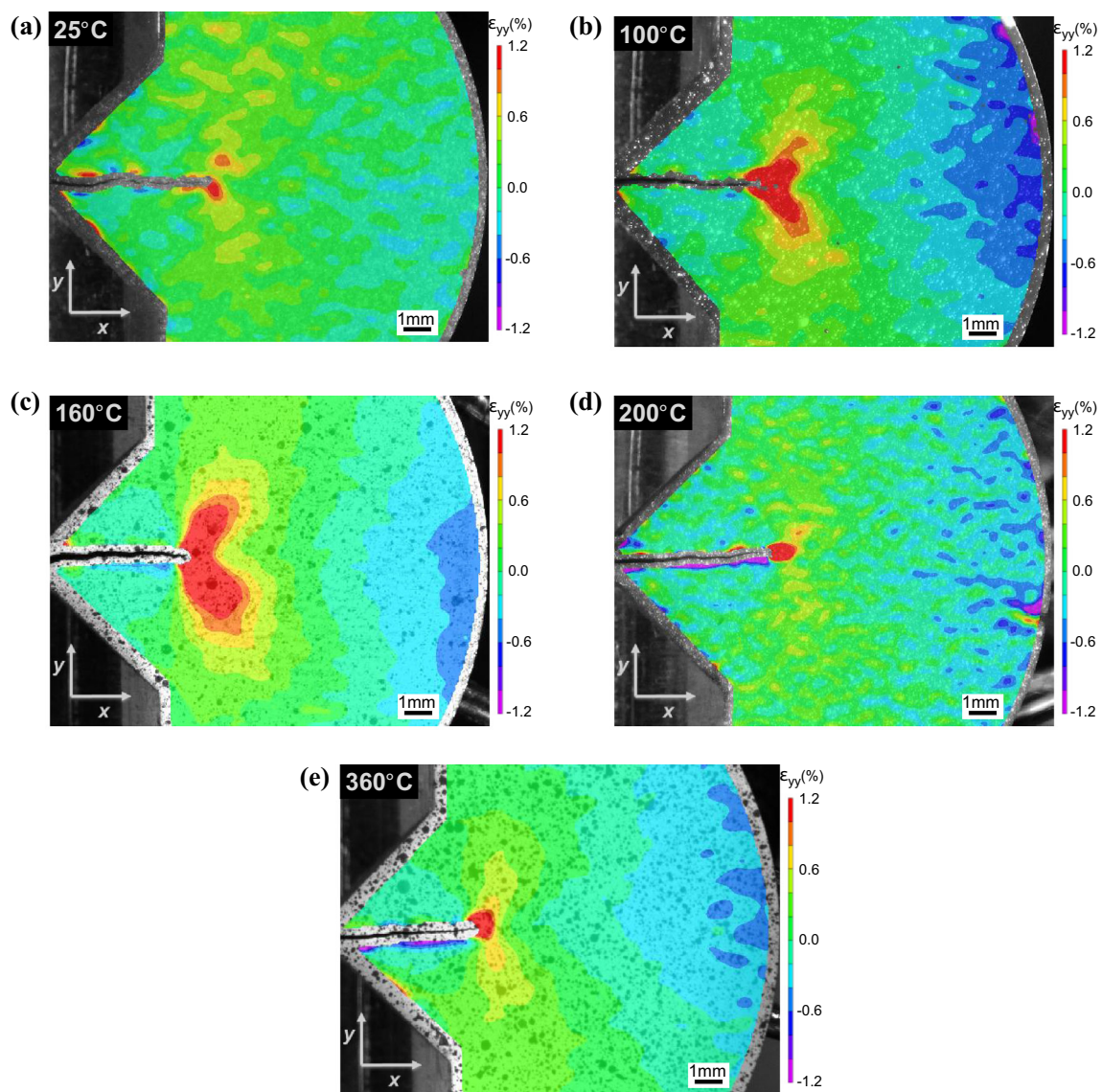


**Fig. 6** Strain ( $\epsilon_{yy}$ ) contour plots at the onset of crack growth for the DCT specimens of the hot extruded, polycrystalline Ni<sub>50.3</sub>Ti<sub>29.7</sub>Hf<sub>20</sub> high temperature shape memory alloy, obtained using DIC at different

test temperatures: **a** 25 °C, **b** 100 °C, **c** 160 °C, **d** 200 °C, and **e** 360 °C. For the ease of comparison, the color bar is fixed for all temperatures so that the red color approximates the inelastic zone



ease of comparison, the color bar is fixed for all testing temperatures so that the red color approximates the inelastic zone. The results at different temperatures are presented in Fig. 6. As can be seen in the figure, at 25 °C, the inelastic zone is relatively small, which matches with the trends in Fig. 5. At 100 °C, there is an increase in the size of the inelastic deformation zone. At 160 °C, there is a noticeable increase in the inelastic zone size, due to the SIM transformation. This can be rationalized using the observations in the uniaxial stress–strain response at 160 °C, according to which the inelastic deformation mechanism, in this case, martensitic transformation, starts at a significantly lower stress/strain values compared to the detwinning mechanism in martensite. At 200 °C, the transformation zone becomes relatively small because at this temperature the transformation is triggered at a higher stress value. Lastly, at 360 °C, the inelastic deformation zone is comparable in size to that at 25 °C.

Comparing the DIC results to the fracture toughness values, one can see that the trend in the temperature evolution in the inelastic deformation zone size matches well with the temperature evolution of the fracture toughness values. This explains the higher fracture toughness value for the samples undergoing SIM transformation, especially at 160 °C, where the material undergoes phase transformation at early stages of loading (Fig. 3a) and dissipates much more energy than martensite detwinning and plastic deformation of austenite.

### Comparison of Fracture Surfaces from Different Temperature Failures

The fracture surfaces of the all failed DCT samples were investigated using SEM at room temperature in order to identify the signature fracture characteristics. The results are presented in Fig. 7. It can be seen that there is a

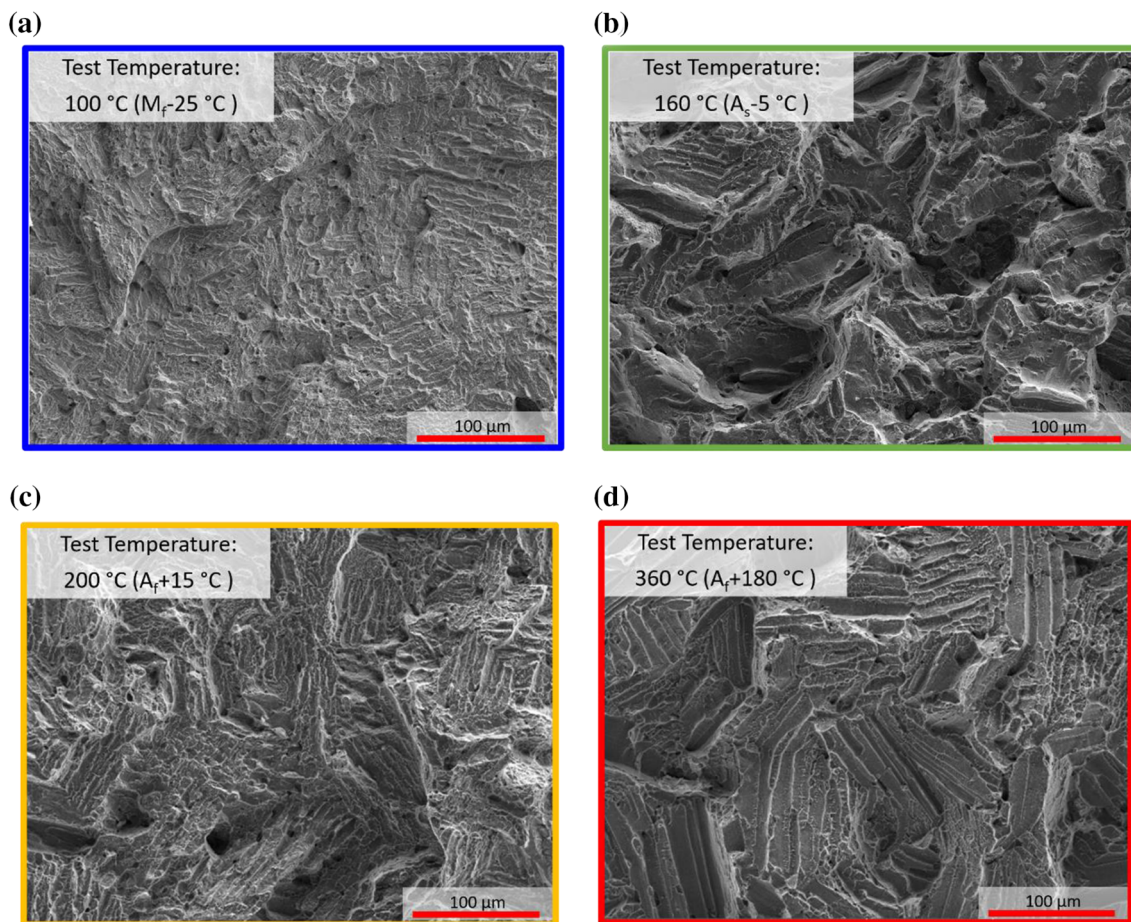


**Fig. 7** Fracture surfaces of the hot extruded, polycrystalline Ni<sub>50.3</sub>-Ti<sub>29.7</sub>Hf<sub>20</sub> DCT specimens taken using an SEM at room temperature: **a** in the samples tested at 100 °C, the fracture surface is relatively flat indicating quasi-cleavage fracture; **b** for the samples tested at 160 °C, the fracture surface features noticeably more dimples indicating much

higher energy dissipation for fracture; **c** for the 200 °C samples, the surfaces seem to exhibit a striated pattern, which is believed to be martensite lathes forming upon cooling inside the larger austenite grains; and **d** for the samples tested at 360 °C, the surface is jagged, and has evidence of inter-granular fracture

difference in the fracture surface morphology at different testing temperatures, which is characterized by either cleavage or micro-void coalescence, or a combination of both. At lower temperatures (25 and 100 °C), the fracture surfaces are much flatter, evidence of quasi-cleavage, transgranular fracture (Fig. 7a). As the temperature increases into the range where SIM transformation takes place (at 160 °C), the fracture surfaces become dimpled and show evidence of ductile fracture (Fig. 7b). As the temperature increases to 200 °C and 360 °C, the fracture surfaces show increasing characteristics of intergranular fracture (Fig. 7c, d), likely to be along the austenite grain boundaries. The repeating structures on the fracture surface which look like parallel bands in these figures, should be bundles of martensite lathes, based on the martensite twin size observed in Fig. 2, that form upon cooling down from the austenitic phase, as these SEM micrographs were taken at room temperature, and not at the temperature of the fracture toughness experiments. Overall, the fracture surface morphologies follow the same temperature trends observed in the fracture toughness experiments and DIC observations, where the SIM transformation leads to the most energy dissipation during the crack growth.

## Summary and Conclusions

In the present study, the fracture behavior of a Ni-rich  $\text{Ni}_{50.3}\text{Ti}_{29.7}\text{Hf}_{20}$  (at.%) HTSMA was investigated at different temperatures using disk-shaped compact tension specimens: below  $M_f$ , above  $M_s$  but below  $M_d$ , and above  $M_d$ , in order to determine the fracture toughnesses of martensitic, martensitically transforming austenitic, and plastically deforming austenitic phases, respectively. Fracture behavior was observed to be highly temperature/phase dependent. The stress-induced martensite (SIM) transformation was found to be a toughening mechanism, increasing the fracture toughness in the present NiTiHf HTSMA, and resulting in stable crack growth when the temperature is close to  $M_s$ . This is in contrast to the fracture toughness values of similar phases in binary equiatomic NiTi SMAs, where martensitic and martensitically transforming austenitic phases experience the same fracture toughness values near the transformation temperatures while plastically deforming austenitic phase exhibits much higher fracture toughness. The apparent toughening via the SIM transformation in the NiTiHf HTSMA is due to the differences in the strain hardening behavior of the martensite detwinning, SIM transformation, and austenite plastic deformation regimes, leading to different sizes of inelastic deformation zones at the crack tip and thus different energy dissipation levels. This toughening mechanism is less significant when the stress required for SIM

transformation is higher at higher temperatures. Digital Image Correlation was implemented to monitor the extent of the inelastic deformation zones near the crack tip, which match well with the observations in temperature evolution of the fracture toughness values. The inelastic zones at temperatures where the SIM transformation is active before failure were found to be larger than at temperatures where only one phase is present, or the stress required to form SIM is very high.

**Acknowledgements** This study was supported by the US Air Force Office of Scientific Research, under Grant No. FA9550-18-1-0276 and the National Science Foundation under Grant No. CMMI-1917367. B. Young acknowledges the support from the 2017 SMST Fellowship. The authors also acknowledge the NASA Glenn Research Center for providing the material used in this work. The authors acknowledge Dr. Baxevanis for the valuable discussions on the fracture toughness measurement method.

## References

- Lagoudas DC (2008) Shape memory alloys: modeling and engineering applications. Springer, Berlin
- Hartl DJ, Lagoudas DC (2007) Aerospace applications of shape memory alloys. *Proc Inst Mech Eng Part G J Aerosp Eng* 221(4):535–552
- Tobushi H, Kimura K, Iwanaga H, Cahoon JR (1990) Basic research on shape memory alloy heat engine (output power characteristics and problems in development). *JSME Int J* 33:263–268
- Buehler WJ, Gilfrich JV, Wiley RC (1963) Effect of low-temperature phase changes on the mechanical properties of alloys near composition TiNi. *J Appl Phys* 34(5):1475–1477
- Umale T, Salas D, Tomes B, Arroyave R, Karaman I (2019) The effects of wide range of compositional changes on the martensitic transformation characteristics of NiTiHf shape memory alloys. *Ser Mater* 161:78–83
- Ma J, Karaman I, Noebe RD (2010) High temperature shape memory alloys. *Int Mater Rev* 55(5):257–315
- Benafan O, Noebe RD, Padula SA, Vaidyanathan R (2012) Microstructural response during isothermal and isobaric loading of a precipitation-strengthened Ni29.7-Ti-20Hf high-temperature shape memory alloy. *Metall Mater Trans A* 43(12):4539–4552
- Saghaian SM, Karaca HE, Tobe H, Souri M, Noebe R, Chumlyakov YI (2015) Effects of aging on the shape memory behavior of Ni-rich  $\text{Ni}_{50.3}\text{Ti}_{29.7}\text{Hf}_{20}$  single crystals. *Acta Mater* 87:128–141
- Santamarta R, Arróyave R, Pons J, Evirgen A, Karaman I, Karaca HE, Noebe RD (2013) TEM study of structural and microstructural characteristics of a precipitate phase in Ni-rich Ni–Ti–Hf and Ni–Ti–Zr shape memory alloys. *Acta Mater* 61(16):6191–6206
- Evirgen A (2014) Microstructural characterization and shape memory response of Ni-Rich NiTiHf and NiTiZr high temperature shape memory alloys. Doctoral Dissertation, Texas A&M University
- Belbasi M, Salehi MT (2014) Influence of chemical composition and melting process on hot rolling of NiTiHf shape memory alloy. *J Mater Eng Perform* 23(7):2368–2372
- Bigelow GS, Garg A, Padula SA, Gaydos DJ, Noebe RD (2011) Load-biased shape-memory and superelastic properties of a

- precipitation strengthened high-temperature Ni<sub>50.3</sub>Ti<sub>29.7</sub>Hf<sub>20</sub> alloy. *Scr Mater* 64(8):725–728
13. Evirgen A, Pons J, Karaman I, Santamarta R, Noebe RD (2018) H-Phase precipitation and martensitic transformation in Ni-rich Ni–Ti–Hf and Ni–Ti–Zr high-temperature shape memory alloys. *Shape Mem Superelast* 4(1):85–92
  14. Evirgen A, Karaman I, Santamarta R, Pons J, Hayrettin C, Noebe RD (2016) Relationship between crystallographic compatibility and thermal hysteresis in Ni-rich NiTiHf and NiTiZr high temperature shape memory alloys. *Acta Mater* 121:374–383
  15. Evirgen A, Karaman I, Santamarta R, Pons J, Noebe RD (2015) Microstructural characterization and shape memory characteristics of the Ni<sub>50.3</sub>Ti<sub>34.7</sub>Hf<sub>15</sub> shape memory alloy. *Acta Mater* 83:48–60
  16. Evirgen A, Karaman I, Noebe RD, Santamarta R, Pons J (2013) Effect of precipitation on the microstructure and the shape memory response of the Ni<sub>50.3</sub>Ti<sub>29.7</sub>Zr<sub>20</sub> high temperature shape memory alloy. *Scr Mater* 69(5):354–357
  17. Evirgen A, Basner F, Karaman I, Noebe RD, Pons J, Santamarta R (2012) Effect of aging on the martensitic transformation characteristics of a Ni-rich NiTiHf high temperature shape memory alloy. *Funct Mater Lett* 5(4):1250038
  18. Karaca HE, Acar E, Tobe H, Saghaian SM (2014) NiTiHf-based shape memory alloys. *Mater Sci Technol* 30(13):1530–1544
  19. Saghaian SM, Karaca HE, Sourji M, Turabi AS, Noebe RD (2010) Tensile shape memory behavior of Ni<sub>50.3</sub>Ti<sub>29.7</sub>Hf<sub>20</sub> high temperature shape memory alloys. *Mater Des* 101:340–345
  20. Shukla D, Noebe RD, Stebner AP (2013) Empirical study of the multiaxial, thermomechanical behavior of NiTiHf shape memory alloys, vol NASA/TM-20130216619. NASA, Cleveland, OH
  21. Benafan O (2012) Deformation and phase transformation processes in polycrystalline NiTi and NiTiHf high temperature shape memory alloys. Doctoral Dissertation, University of Central Florida
  22. Hayrettin C (2017) Actuation fatigue and fracture of shape memory alloys. Doctoral Dissertation, Texas A&M University
  23. Karakoc O, Demblon A, Wheeler RW, Lagoudas DC, Karaman I (2019) Effects of testing parameters on the fatigue performance NiTiHf high temperature shape memory alloys. In: AIAA Scitech 2019 Forum, 2019, p 0416
  24. Karakoc O, Hayrettin C, Canadinc D, Karaman I (2018) Role of applied stress level on the actuation fatigue behavior of NiTiHf high temperature shape memory alloys. *Acta Mater* 153:156–168
  25. Karakoc O, Hayrettin C, Evirgen A, Santamarta R, Canadinc D, Wheeler RW, Wang SJ, Lagoudas DC, Karaman I (2019) Role of microstructure on the actuation fatigue performance of Ni-Rich NiTiHf high temperature shape memory alloys. *Acta Mater* 175:107–120
  26. Hayrettin C, Karakoc O, Karaman I, Mabe JH, Santamarta R, Pons J (2019) Two way shape memory effect in NiTiHf high temperature shape memory alloy tubes. *Acta Mater* 163:1–13
  27. Russell SM, Sczerzenie F (1994) Engineering considerations in the application of NiTiHf and NiAl as practical high-temperature shape memory alloys. *MRS Proc* 360:455
  28. Babacan N, Bilal M, Hayrettin C, Liu J, Benafan O, Karaman I (2018) Effects of cold and warm rolling on the shape memory response of Ni<sub>50</sub>Ti<sub>30</sub>Hf<sub>20</sub> high-temperature shape memory alloy. *Acta Mater* 157:228–244
  29. Kockar B, Karaman I, Kim JI, Chumlyakov Y (2006) A method to enhance cyclic reversibility of NiTiHf high temperature shape memory alloys. *Scr Mater* 54(12):2203–2208
  30. Moholt M, Benafan O (2017) Spanwise Adaptive Wing. Presented at the 3rd Annual Convergent Aeronautics Solutions Showcase and Innovation Faire, VA
  31. Holtz RL, Sadananda K, Imam MA (1999) Fatigue thresholds of Ni-Ti alloy near the shape memory transition temperature. *Int J Fatigue* 21:S137–S145
  32. Robertson SW, Ritchie RO (2007) In vitro fatigue–crack growth and fracture toughness behavior of thin-walled superelastic Nitinol tube for endovascular stents: a basis for defining the effect of crack-like defects. *Biomaterials* 28(4):700–709
  33. Daly S, Miller A, Ravichandran G, Bhattacharya K (2007) An experimental investigation of crack initiation in thin sheets of nitinol. *Acta Mater* 55(18):6322–6330
  34. Gollerthan S, Young ML, Baruj A, Frenzel J, Schmahl WW, Eggeler G (2009) Fracture mechanics and microstructure in NiTi shape memory alloys. *Acta Mater* 57(4):1015–1025
  35. Ahadi A, Sun Q (2016) Grain size dependence of fracture toughness and crack-growth resistance of superelastic NiTi. *Scr Mater* 113:171–175
  36. Katanchi B, Choupani N, Khalil-Allafi J, Tavangar R, Baghani M (2018) Mixed-mode fracture of a superelastic NiTi alloy: experimental and numerical investigations. *Eng Fract Mech* 190:273–287
  37. Robertson SW, Pelton AR, Ritchie RO (2012) Mechanical fatigue and fracture of Nitinol. *Int Mater Rev* 57(1):1–37
  38. Maletta C, Sgambitterra E, Furgiuele F (2013) Crack tip stress distribution and stress intensity factor in shape memory alloys. *Fatigue Fract Eng Mater Struct* 36(9):903–912
  39. Melton KN, Mercier O (1981) The mechanical properties of NiTi-based shape memory alloys. *Acta Metall* 29(2):393–398
  40. Robertson SW, Ritchie RO (2008) A fracture-mechanics-based approach to fracture control in biomedical devices manufactured from superelastic Nitinol tube. *J Biomed Mater Res Part B* 84B(1):26–33
  41. Luo J, He J, Wan X, Dong T, Cui Y, Xiong X (2016) Fracture properties of polycrystalline NiTi shape memory alloy. *Mater Sci Eng A* 653:122–128
  42. ASTM Standard E399 (2011) Standard test method for linear-elastic plane-strain fracture toughness K<sub>Ic</sub> of metallic materials. ASTM International, West Conshohocken, PA
  43. Baxevanis T, Chemisky Y, Lagoudas DC (2012) Finite element analysis of the plane strain crack-tip mechanical fields in pseudoelastic shape memory alloys. *Smart Mater Struct* 21(9):094012
  44. Baxevanis T, Lagoudas D (2012) A mode I fracture analysis of a center-cracked infinite shape memory alloy plate under plane stress. *Int J Fract* 175(2):151–166
  45. Falvo A, Furgiuele F, Leonardi A, Maletta C (2009) Stress-induced martensitic transformation in the crack tip region of a NiTi alloy. *J Mater Eng Perform* 18(5):679–685
  46. Haghgouyan B, Jape S, Baxevanis T, Karaman I, Lagoudas DC (2019) Stable crack growth in NiTi shape memory alloys: 3D finite element modeling and experimental validation. *Smart Mater Struct* 28(6):064001
  47. Haghgouyan B, Karaman I, Jape S, Solomou A, Lagoudas DC (2018) Crack growth behavior in NiTi shape memory alloys under mode-I isothermal loading: effect of stress state. ASME 2018 Conference on Smart Materials, Adaptive Structures and Intelligent Systems: V002T02A013-V002T02A013
  48. Jape S, Baxevanis T, Lagoudas DC (2016) Stable crack growth during thermal actuation of shape memory alloys. *Shape Mem Superelast* 2(1):104–113
  49. Sgambitterra E, Maletta C, Furgiuele F, Sehitoglu H (2018) Fatigue crack propagation in [0 1 2] NiTi single crystal alloy. *Int J Fatigue* 112:9–20
  50. Sgambitterra E, Maletta C, Magarò P, Renzo D, Furgiuele F, Sehitoglu H (2019) Effects of temperature on fatigue crack propagation in pseudoelastic NiTi shape memory alloys. *Shape Memory Superelast*

51. Haghgouyan B, Hayrettin C, Baxevanis T, Karaman I, Lagoudas DC (2019) Fracture toughness of NiTi—Towards establishing standard test methods for phase transforming materials. *Acta Mater* 162:226–238
52. ASTM Standard E1820 (2014) Standard Test Method for Measurement of Fracture Toughness. ASTM International, West Conshohocken, PA
53. Haghgouyan B, Shafaghi N, Aydiner CC, Anlas G (2016) Experimental and computational investigation of the effect of phase transformation on fracture parameters of an SMA. *Smart Mater Struct* 25(7):075010
54. Maletta C, Sgambitterra E, Niccoli F (2016) Temperature dependent fracture properties of shape memory alloys: novel findings and a comprehensive model. *Sci Rep* 6(1):17
55. Haghgouyan B, Young B, Karaman I, Lagoudas DC (2019) Fracture toughness of martensitic NiTiHf high-temperature shape memory alloy. *Behavior and Mechanics of Multifunctional Materials XIII*. 10968:109680A
56. Amin-Ahmadi B, Noebe RD, Stebner AP (2019) Crack propagation mechanisms of an aged nickel-titanium-hafnium shape memory alloy. *Scr Mater* 159:85–88
57. Chen Y, Tyc O, Molnárová O, Heller L, Šittner P (2019) Tensile deformation of superelastic NiTi wires in wide temperature and microstructure ranges. *Shape Mem Superelast* 5(1):42–62
58. Paul PP, Fortman M, Paranjape HM, Anderson PM, Stebner AP, Brinson LC (2018) Influence of structure and microstructure on deformation localization and crack growth in NiTi shape memory alloys. *Shape Mem Superelast* 4(2):285–293
59. Santamarta R, Evirgen A, Perez-Sierra AM, Pons J, Cesari E, Karaman I, Noebe RD (2015) Effect of thermal treatments on Ni–Mn–Ga and Ni-Rich Ni–Ti–Hf/Zr high-temperature shape memory alloys. *Shape Mem Superelast* 1(4):418–428
60. Gall K, Yang N, Sehitoglu H, Chumlyakov YI (2001) Fracture of precipitated NiTi shape memory alloys. *Int J Fract* 109(2):189–207
61. Robertson SW, Mehta A, Pelton AR, Ritchie RO (2007) Evolution of crack-tip transformation zones in superelastic Nitinol subjected to in situ fatigue: a fracture mechanics and synchrotron X-ray microdiffraction analysis. *Acta Mater* 55(18):6198–6207
62. Karaca HE, Saghaian SM, Ded G, Tobe H, Basaran B, Maier HJ, Noebe RD, Chumlyakov YI (2013) Effects of nanoprecipitation on the shape memory and material properties of an Ni-rich NiTiHf high temperature shape memory alloy. *Acta Mater* 61(19):7422–7431
63. Benafan O, Garg A, Noebe RD, Bigelow GS, Padula SA, Gaydos DJ, Schell N, Mabe JH, Vaidyanathan R (2014) Mechanical and functional behavior of a Ni-rich Ni<sub>50.3</sub>Ti<sub>29.7</sub>Hf<sub>20</sub> high temperature shape memory alloy. *Intermetallics* 50:94–107
64. Surikova NS, Chumlyakov YI (2000) Mechanisms of plastic deformation of the titanium nickelide single crystals. *Phys Metals Metallogr* 89(2):196–205
65. Sehitoglu H, Karaman I, Anderson R, Zhang X, Gall K, Maier HJ, Chumlyakov Y (2000) Compressive response of NiTi single crystals. *Acta Mater* 48(13):3311–3326
66. Sehitoglu H, Hamilton R, Canadinc D, Zhang XY, Gall K, Karaman I, Chumlyakov Y, Maier HJ (2003) Detwinning in NiTi alloys. *Metall Mater Trans A* 34(1):5–13
67. Chumlyakov YI, Kireeva IV, Panchenko EY, Timofeeva EE, Pobedennaya ZV, Chusov SV, Karaman I, Maier H, Cesari E, Kirillov VA (2008) High-temperature superelasticity in CoNiGa, CoNiAl, NiFeGa, and TiNi monocrystals. *Russ Phys J* 51(10):1016–1036
68. Benafan O, Gaydos DJ (2017) High temperature shape memory alloy Ni<sub>50.3</sub>Ti<sub>29.7</sub>Hf<sub>20</sub> torque tube actuators. *Smart Mater Struct* 26(9):095002
69. Benafan O, Gaydos DJ (2018) Constant-torque thermal cycling and two-way shape memory effect in Ni<sub>50.3</sub>Ti<sub>29.7</sub>Hf<sub>20</sub> torque tubes. *Smart Mater Struct* 27(7):075035
70. Makkar J, Baxevanis T (2019) Notes on the experimental measurement of fracture toughness of shape memory alloys. *J Intell Mater Syst Struct* 1-9

**Publisher's Note** Springer Nature remains neutral with regard to jurisdictional claims in published maps and institutional affiliations.